Research Article

Improved Photocatalytic Activity of TiO_2 through $MnFe_2O_4$/Chitosan–Alginate Doping for Procion red MX-5B Degradation and Ecotoxicity Evaluation

Poedji Loekitowati Hariani*, Addy Rachmat, Desnelli, Annisah Falihah and Adelia
Department of Chemistry, Faculty of Mathematics and Natural Sciences, Universitas Sriwijaya, Jalan Palembang-Prabumulih, Indralaya, Ogan Ilir, Indonesia

Salni
Department of Biology, Faculty of Mathematics and Natural Sciences, Universitas Sriwijaya, Jalan Palembang-Prabumulih, Indralaya, Ogan Ilir, Indonesia

Nabila Aprianti
Research Center for Photonics, National Research and Innovation Agency (BRIN), South Tangerang, Banten, Indonesia

* Corresponding author. E-mail: puji_lukitowati@mipa.unsri.ac.id DOI: 10.14416/j.asep.2026.03.001
Received: 19 October 2025; Revised: 7 December 2025; Accepted: 29 December 2025; Published online: 5 March 2026

Abstract
The development of photocatalytic materials for organic pollutant degradation has continued to advance. In this study, a $MnFe_2O_4$/Chitosan–Alginate@TiO_2 composite was synthesized, in which magnetic $MnFe_2O_4$ was encapsulated within a chitosan–alginate polymer matrix and doped with TiO_2. The composite's crystal structure, morphology, elemental composition, optical, and magnetic properties were characterized using XRD, SEM–EDX, UV–DRS, and VSM analyses. Optimization of Procion Red MX-5B (PRD) dye degradation was performed using Response Surface Methodology (RSM), with PRD concentration, pH, and irradiation time as independent variables. The composite exhibited strong magnetic behavior (magnetic moment: 44.63 emu/g) and a narrow band gap (2.20 eV). The photocatalytic degradation followed a quadratic model, with all variables showing significant effects (p-value < 0.05). The predicted optimal conditions, which include a PRD concentration of 45 mg/L, pH 3.3, and 59 min of irradiation time, resulted in a measured degradation efficiency of 99.71%. The composite demonstrated excellent stability after six recycling cycles. TOC removal of 84.30% confirmed substantial mineralization into inorganic compounds, such as CO_2 and H_2O, while ecotoxicity tests using green gram seeds germination indicated that the degradation products were non-toxic.

Keywords: Ecotoxicity, $MnFe_2O_4$/Chitosan–Alginate@TiO_2 composite, Procion red MX-5B, Quadratic model, TOC

1 Introduction

Dyes used in coloring processes can be classified into two main types: natural dyes and synthetic dyes. Among them, synthetic dyes are more commonly used in industrial applications because of their bright and stable colors, excellent durability, and greater versatility compared to natural dyes [1]. Currently, more than 10,000 types of synthetic dyes are employed across various industries. The textile and dyeing industries generate large volumes of highly concentrated wastewater. During the dyeing process, approximately 20–50% of the dye is lost to the effluent, making the textile industry responsible for about 54% of global dye pollution [2]–[4].

Among these pollutants, azo dyes represent the largest class of synthetic dyes, characterized by the presence of an azo group (-C–N=N–C-) linking two aromatic rings. These compounds pose serious environmental and ecological risks due to their low

biodegradability and high stability. Azo dyes can persist in aquatic systems, reducing light penetration, inhibiting photosynthesis, and exhibiting toxic effects on microorganisms and aquatic life, ultimately leading to biodiversity loss. Moreover, some azo dyes can degrade into aromatic amines, which are toxic, mutagenic, and carcinogenic [5]–[7].

Procion Red MX–5B (PRD) is a reactive azo dye with the molecular formula $C_{23}H_{11}Cl_2N_6Na_3O_{10}S_3$. It is highly water–soluble and widely applied in dyeing of various fibers such as cellulose, nylon, silk, wool, cotton, and linen [8], [9]. The presence of aromatic rings and conjugated functional groups (including azo, naphthalene, and triazine moieties) contributes to its chemical stability, making PRD resistant to natural degradation and a persistent environmental pollutant.

A range of methods has been utilized to eliminate dye pollutants from wastewater, such as electrochemical treatment [10], adsorption [11], biosorption [12], coagulation [13], and ozonation [14]. Among these, photocatalytic degradation has emerged as a promising and environmentally friendly approach. It requires low energy input and can mineralize complex organic pollutants into simple, non–toxic compounds such as CO_2, H_2O, and inorganic ions [9]. In contrast, methods like adsorption merely transfer pollutants between phases without decomposing them, and often face challenges related to regeneration, recycling, and the formation of sludge or secondary pollutants [15], [16].

Among various photocatalysts, titanium dioxide (TiO_2) stands out due to its chemical stability, low cost, environmental benignity, non–toxicity, and ease of modification or doping, which enhances its ability to generate oxidative radicals for pollutant degradation [17], [18]. However, TiO_2 exhibits several limitations: its wide band gap (>3 eV) restricts light absorption to the UV region [19], [20], and the recombination of photogenerated electron–hole (e^-/h^+) pairs often reduces photocatalytic efficiency [21], [22]. Additionally, the recovery of TiO_2 nanoparticles after treatment is difficult due to their small size, posing a risk of secondary contamination in treated water [23].

Several researchers have modified TiO_2 with various materials to enhance its photocatalytic performance. For example, $NiFe_2O_4$-doped TiO_2, synthesized at calcination temperatures of 500, 700, and 900 °C, exhibits a narrower band gap (1.9–2.5 eV) compared to pure TiO_2 [24]. Similarly, polyaniline (PANI) doping at different concentrations reduces the TiO_2 band gap to 1.91–2.18 eV [25]. Incorporating organic compounds such as polyaniline, chitosan, alginate, graphene, or biochar can enhance TiO_2 stability, prevent nanoparticle agglomeration, and broaden its light absorption beyond the UV region [26]–[28].

Doping TiO_2 with ferrite compounds (MFe_2O_4, where M = Mn, Co, Ni, Zn, Cu, etc.) has also been extensively investigated, as these materials impart magnetic and electronic properties absent in pure TiO_2. $MnFe_2O_4$–TiO_2 composites possess multiple functional properties, including the inhibition of electron–hole recombination, increased activity under visible light, and improved efficiency of charge carrier separation [29], [30]. $MnFe_2O_4$, a spinel ferrite, has attracted considerable interest due to its high magnetic strength, chemical stability, large specific surface area, and antibacterial activity [31]. To further improve its photocatalytic performance, natural polymers such as chitosan and alginate can be incorporated as supporting matrices. Chitosan, a biodegradable and biocompatible biopolymer containing $–NH_2$ and –OH functional groups, facilitates pollutant adsorption and interaction with semiconductor surfaces prior to degradation. Alginate, rich in carboxyl (–COOH) groups, contributes to nanoparticle stabilization and porosity enhancement, promoting more efficient contact between the photocatalyst and dye molecules. Both polymers are non–toxic and environmentally friendly [32–34].

$MnFe_2O_4$ and TiO_2 form a p–n heterojunction system that facilitates efficient charge separation. Under light irradiation, both semiconductors generate electron–hole pairs. Electrons in the conduction band of $MnFe_2O_4$ migrate to the conduction band of TiO_2, while holes migrate from the valence band of TiO_2 to $MnFe_2O_4$. This charge redistribution inhibits electron–hole recombination and enhances the formation of reactive radicals, thus improving the overall photocatalytic performance. The mechanism of this system corresponds to a type 2 heterojunction, in which charge separation occurs based on the flow of electrons and holes toward materials with more stable energy levels [35], [36].

The development of a $MnFe_2O_4$/Chitosan–Alginate@TiO_2 composite as a photocatalyst combining three components has the advantages of magnetic $MnFe_2O_4$, biopolymer (chitosan–alginate) for improved adsorption capacity, and TiO_2 for photocatalytic activity. This synergistic structure provides greater degradation efficiency and enables easy separation and reuse of the material.

In this study, $MnFe_2O_4$ was synthesized and dispersed within a Chitosan–Alginate matrix, followed by doping onto TiO_2 to form a $MnFe_2O_4$/Chitosan–

Alginate@TiO_2 composite. The composite was evaluated as a photocatalyst for the degradation of PRD using Response Surface Methodology (RSM). Furthermore, an ecotoxicity test using plant-based bioindicators was conducted to assess the environmental safety of the degradation products and their potential effects on living organisms. Green gram seeds were utilized for the ecotoxicity test.

2 Materials and Methods

2.1 *Materials*

All chemicals employed were of analytical grade, and distilled water served as the solvent for all experimental procedures. The materials included anhydrous $FeCl_3$ (≥97%), $MnCl_2.4H_2O$ (≥98%), NaOH, $CaCl_2$, ethanol, chitosan (75–85% deacetylation), sodium alginate, glacial acetic acid (≥99.7%), TiO_2, and Procion Red MX–5B, all purchased from Sigma Aldrich (Germany).

2.2 *Synthesis of $MnFe_2O_4$*

$MnFe_2O_4$ was synthesized using the co–precipitation method [37]. Briefly, 3.244 g $FeCl_3$ was dissolved in 200 mL of distilled water, followed by the addition of 1.979 g $MnCl_2.4H_2O$ (molar ratio Fe: Mn = 2:1). The solution was stirred for 15 min, after which 2 M NaOH was added dropwise under continuous stirring and heating at 80 °C until the pH reached 11. The precipitate obtained was washed several times with distilled water and ethanol until a neutral pH was achieved. Finally, the product was calcined at 500 °C for 3 h to obtain $MnFe_2O_4$ powder.

2.3 *Synthesis of $MnFe_2O_4$/Chitosan–Alginate Composite*

Chitosan (1.0 g) was dissolved in 5 mL acetic acid and 50 mL of 2% (w/v) $CaCl_2$ solution, stirred for 24 h. Separately, sodium alginate (1.0 g) was dissolved in 50 mL of distilled water and stirred for 2 h at room temperature. The alginate solution was then added slowly to the chitosan solution and stirred at 40 °C for 2 h to form a homogeneous polymer matrix. $MnFe_2O_4$ (0.5 g) was gradually added and stirred for 6 h. The resulting mixture was filtered and dried at 80 °C for 36 h to obtain the $MnFe_2O_4$/Chitosan–Alginate.

2.4 *Synthesis of $MnFe_2O_4$/Chitosan–Alginate@TiO_2 Composite*

The $MnFe_2O_4$/Chitosan–Alginate@TiO_2 composite was synthesized using 2 mixtures, namely $MnFe_2O_4$/Chitosan-alginate and TiO_2. The procedure for the synthesis of $MnFe_2O_4$/Chitosan–Alginate was in accordance with the previous procedure. A total of 1.0 g of TiO_2 was added to the mixture, followed by sonication until the suspension was homogeneous. The composite precipitate was filtered and washed several times with distilled water. It was then dried in an oven for 24 h at 100 °C.

2.5 *Material characterization*

The crystal structure was analyzed by X-ray diffraction (XRD, PANalytical X'Pert Pro) using Cu Kα radiation (λ = 0.15406 nm) over a 2θ range of 10–90°. The surface morphology and elemental composition were examined using Scanning Electron Microscopy coupled with Energy-Dispersive X-ray Spectroscopy (SEM–EDX, Hitachi FlexSEM 1000). UV–Vis Diffuse Reflectance Spectroscopy (UV–DRS, Cary 60, version 2.00) was used to determine the optical absorption and band gap energy. The magnetic properties were measured using a Vibrating Sample Magnetometer (VSM, 1.2H type), in a magnetic field of ±10 kOe with a vibration frequency of 80 Hz. Dye absorbance during photocatalytic tests was determined using a UV–Vis Spectrophotometer (Shimadzu UV–3600), while total organic carbon (TOC) analysis was carried out using a TOC analyzer (Shimadzu AA–7800).

2.6 *Implementation of RSM for optimizing PRD degradation*

Response Surface Methodology (RSM) based on a Central Composite Design (CCD) was employed using Design Expert software to optimize the degradation of PRD. This approach was used to evaluate both the individual and interactive effects of independent variables on the response variable. The three independent variables investigated were PRD concentration (A), pH solution (B), and irradiation time (C).

Photocatalytic degradation was carried out in a photoreactor using a 500 W halogen lamp as a visible–light source, positioned 15 cm from the sample. Each experiment employed 50 mL of PRD solution mixed with 0.05 g of the composite. The suspension was first stirred in the dark for 30 min to allow adsorption–desorption equilibrium. After irradiation, aliquots were collected and the remaining PRD was quantified by measuring absorbance at 542 nm using a UV–Vis

spectrophotometer. The degradation efficiency was calculated from the decrease in dye concentration before and after the photocatalytic reaction.

2.7 *Determination of pHpzc*

The composite's point of zero charge (pHpzc) was measured using the pH drift technique. Briefly, 0.05 g of the composite was mixed with 50 mL of 0.1 M NaCl solution, and the initial pH was adjusted between 2 and 12 using 0.1 M HCl or NaOH. The suspensions were then agitated for 24 h, after which the final pH values were recorded. The pHpzc was identified from the point where the curve of initial pH versus ΔpH intersected [38].

2.8 *Ecotoxicity test*

The ecotoxicity of the degraded PRD solution was evaluated using green gram seeds (*Vigna radiata* L.), following the procedure described in [6]. Before use, the seeds were washed three times with distilled water. A total of thirty seeds were then distributed into three Petri dishes lined with cotton and treated with 10 mL of (i) 5 mg/L PRD solution, (ii) degraded PRD solution (at optimum condition), and (iii) distilled water (control). Dishes were kept at room temperature (28 ± 2°C), under ambient light conditions, and without additional aeration.

Germination was allowed for four days, during which the dishes were periodically moistened with the appropriate test solution to maintain consistent hydration. The dishes were maintained at room temperature for four days to allow germination, with periodic watering using the respective solutions. The effects of the treatments were assessed by measuring germination percentage. Each experiment was conducted three times to ensure reproducibility.

3 Results and Discussion

3.1 *Characterization of $MnFe_2O_4$/Chitosan–Alginate@TiO_2 Composite*

The XRD pattern of $MnFe_2O_4$ exhibits a main diffraction peak at 2θ = 35.09°, which represents the characteristic (311) plane of the spinel structure. This peak appears consistently in $MnFe_2O_4$, $MnFe_2O_4$/Chitosan–Alginate, and $MnFe_2O_4$/Chitosan –Alginate@TiO_2 (Figure 1). The diffraction peaks observed at 2θ = 18.36°, 30.08°, 35.09°, 43.01°, 53.11°, 56.47°, and 61.98° correspond to the (111), (220), (311), (400), (422), (511), and (440) crystal planes of $MnFe_2O_4$, consistent with JCPDS No. 74–2403 [31].

The $MnFe_2O_4$/Chitosan–Alginate shows the same diffraction peaks as pure $MnFe_2O_4$ but with reduced intensity, indicating that the ferrite phase is retained while the amorphous nature of chitosan and alginate suppresses the overall crystallinity. Since chitosan and alginate are amorphous polymers, their weak peaks are generally not visible in XRD spectra. For the $MnFe_2O_4$/Chitosan–Alginate@TiO_2 composite, the diffraction pattern exhibits a combination of peaks originating from both $MnFe_2O_4$ and TiO_2.

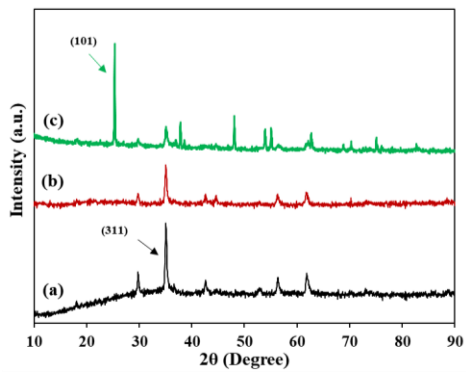

Figure 1: XRD spectra of (a) $MnFe_2O_4$, (b) $MnFe_2O_4$/Chitosan–Alginate, and (c) $MnFe_2O_4$/ Chitosan–Alginate@TiO_2 composite.

TiO_2 has three types of phases, namely anatase, rutile, and brookite phases. In this study, the TiO_2 component is identified as the anatase phase, showing characteristic peaks at 2θ = 25.25° (101), 37.81° (004), 48.01° (200), 53.93° (105), 55.10° (211), and 62.68° (204), matching JCPDS No. 21-1272. The sharp and dominant peak at 2θ = 25.35° confirms the anatase structure, which is known to possess higher photocatalytic activity than the rutile phase [39].

The surface morphology of $MnFe_2O_4$, $MnFe_2O_4$/Chitosan–Alginate, and $MnFe_2O_4$/Chitosan –Alginate@TiO_2 composites is shown in Figure 2. $MnFe_2O_4$ particles appear irregularly spherical and partially agglomerated—a morphology typical of ferrite nanoparticles. In the $MnFe_2O_4$/Chitosan–Alginate composite, the polymer network structure is evident, encapsulating the ferrite nanoparticles and producing a smoother and more homogeneous surface. Upon TiO_2 incorporation, the surface becomes more complex and stratified, indicating strong interaction among $MnFe_2O_4$, the chitosan–alginate matrix, and TiO_2 particles. The presence of TiO_2 is further evidenced by bright white particles distributed within the composite matrix [40].

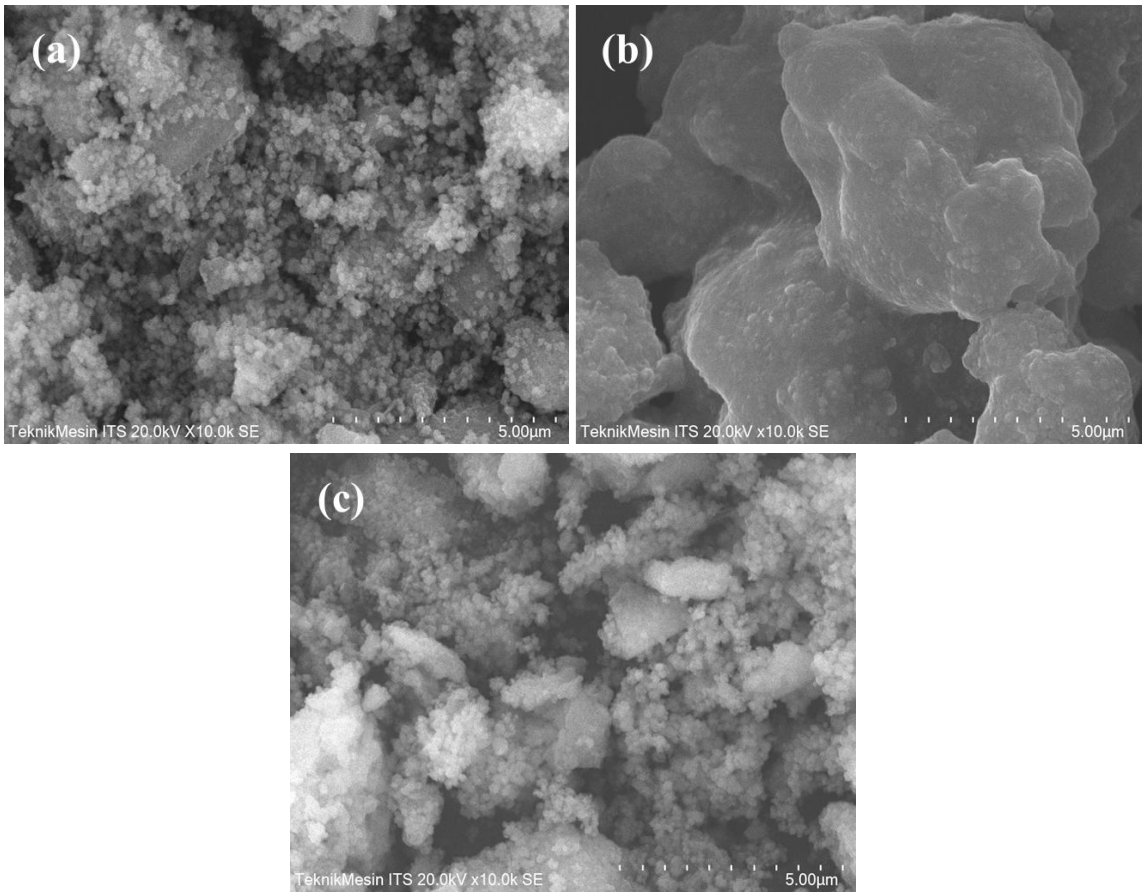

Figure 2: Scanning Electron Microscope (SEM) images of (a) $MnFe_2O_4$, (b) $MnFe_2O_4$/ Chitosan–Alginate, and (c) $MnFe_2O_4$/ Chitosan–Alginate @TiO_2 composite.

Table 1 lists the elemental compositions of $MnFe_2O_4$, $MnFe_2O_4$/Chitosan–Alginate, and $MnFe_2O_4$/Chitosan–Alginate@TiO_2 composites, while the elemental mapping of the $MnFe_2O_4$/Chitosan–Alginate@TiO_2 composite is shown in Figure 3. The mapping results reveal that carbon (C) is uniformly distributed across the surface, indicating that the chitosan–alginate matrix serves as a supporting framework. Oxygen (O) is also evenly dispersed, as it is present in all three components: $MnFe_2O_4$, chitosan–alginate, and TiO_2.

Manganese (Mn) and iron (Fe) appear in relatively low concentrations, likely due to the encapsulation of $MnFe_2O_4$ particles within the chitosan–alginate polymer and the coverage by TiO_2. Nitrogen (N) is detected from the chitosan component in a small percentage. The decrease in the percentage of Fe and Mn elements in the composite compared to $MnFe_2O_4$ and $MnFe_2O_4$/Chitosan–Alginate, accompanied by the detection of Mn, Fe, O, C, N, and Ti elements, indicates that the $MnFe_2O_4$/Chitosan–Alginate@TiO_2 composite was successfully formed. Dispersion of TiO_2 in $MnFe_2O_4$/Chitosan–Alginate can reduce solubility and prevent the release of TiO_2 particles into the environment, thereby reducing the potential for the formation of secondary pollutants.

Table 1: Elemental composition of $MnFe_2O_4$/Chitosan–Alginate@TiO_2 composite based on EDX analysis.

Component	Weight (%)					
	Mn	Fe	O	C	N	Ti
$MnFe_2O_4$	23.96	48.45	27.59	–	–	–
$MnFe_2O_4$/Chitosan–Alginate	14.53	29.74	31.19	22.68	1.86	–
$MnFe_2O_4$/Chitosan–Alginate@TiO_2 composite	8.61	16.39	37.13	19.05	1.97	18.82

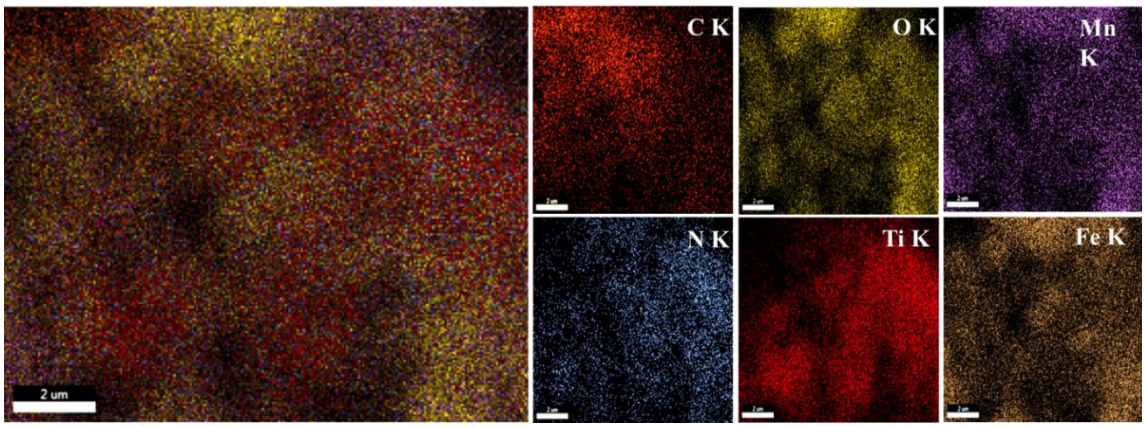

Figure 3: Elemental mapping of $MnFe_2O_4$/Chitosan–Alginate@TiO_2 composite.

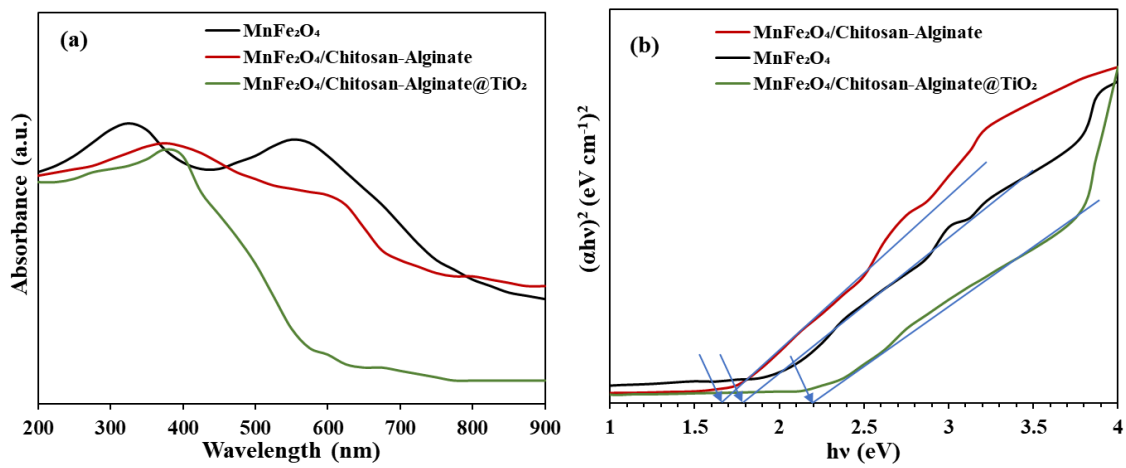

Figure 4: (a) UV–DRS spectra and (b) plot of $(\alpha h\nu)^2$ versus energy (eV) to evaluate the band gap.

Figure 4 presents the UV–Vis absorption spectra and corresponding band gap energies of each material. $MnFe_2O_4$ exhibits two main absorption peaks at approximately 320 nm and 580 nm. After coating with chitosan–alginate, the absorption edge shifts toward longer wavelengths, indicating enhanced light absorption. In the $MnFe_2O_4$/Chitosan–Alginate@TiO_2 composite, a distinct absorption band appears around 380 nm in the UV region, characteristic of the anatase phase of TiO_2. The calculated band gap values are consistent with these spectral shifts, where an extension of the absorption region corresponds to a narrower band gap. Sequentially, the band gaps of $MnFe_2O_4$, $MnFe_2O_4$/Chitosan–Alginate, and $MnFe_2O_4$/Chitosan–Alginate@TiO_2 composite are 1.78 eV, 1.66 eV, and 2.20 eV, respectively. The reduction in band gap after incorporating chitosan–alginate can be attributed to the formation of defect states that introduce intermediate energy levels between the valence and conduction bands. Similar findings were reported for $MnFe_2O_4$ coated with poly(m–aminophenol), where the band gap decreased from 1.80 to 1.70 eV [41].

$MnFe_2O_4$ is classified as a soft magnetic material, characterized by low coercivity (Hc) and relatively high saturation magnetization (Ms). In this study, $MnFe_2O_4$ exhibited an Ms value of 59.30 emu/g (Figure 5). The result aligns with a previous report that obtained 56.49 emu/g for pure $MnFe_2O_4$, whereas doping with N-doped carbon–CuS significantly reduced the magnetization to 5.76 emu/g [42].

A similar trend is observed in this work, where compositing $MnFe_2O_4$ with chitosan–alginate and TiO_2 leads to a decrease in magnetic properties. The reduction is primarily caused by (i) magnetic dilution due to the presence of non-magnetic components (chitosan–alginate and TiO_2) and (ii) the coating effect, which isolates $MnFe_2O_4$ particles, restricts dipolar interactions, and suppresses magnetization. The Ms values of $MnFe_2O_4$/Chitosan–Alginate and

$MnFe_2O_4$/Chitosan–Alginate@TiO_2 are 54.34 emu/g and 44.63 emu/g, respectively. Despite this decrease, the $MnFe_2O_4$/Chitosan–Alginate@TiO_2 composite retains a sufficiently strong magnetic response, allowing facile magnetic separation from aqueous solutions.

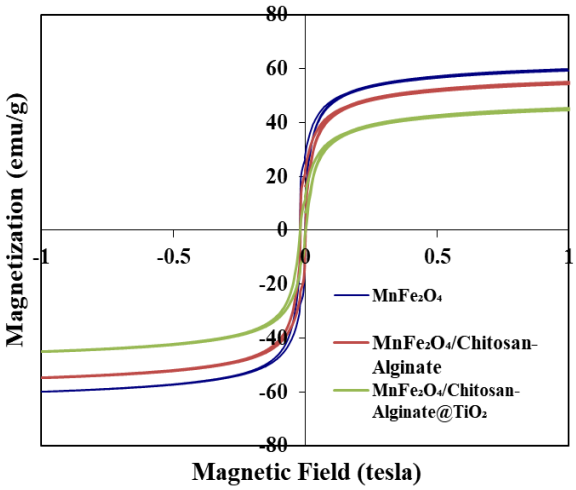

Figure 5: Hysteresis loop of $MnFe_2O_4$, $MnFe_2O_4$/Chitosan–Alginate, and $MnFe_2O_4$/Chitosan –Alginate@TiO_2 composite.

3.2 *Statistical analysis*

The photocatalytic degradation of PRD by the $MnFe_2O_4$/Chitosan–Alginate@TiO_2 composite was analyzed using a statistical–mathematical framework based on RSM to assess and optimize the operational parameters. A CCD was applied to explore the correlation between multiple independent factors and the corresponding response variable. The independent variables considered were PRD concentration (A), pH solution (B), and irradiation time (C).

The quadratic model proved to be the most appropriate model for representing the experimental data obtained. This is evident from the very small difference between the actual and predicted values, which ranged from 0.03% to 4.72%. This relatively low deviation range confirms the model's high accuracy. These results indicate that the quadratic model is able to describe the relationship between variables well and provides estimates that are close to the actual results. This low deviation reflects the strong agreement between experimental data and model predictions (Table 2).

The quadratic model's relevance was further examined using ANOVA, which provided an F–value and *p*–value. A model is considered more significant when the F–value is high and the p–value is low, with statistical significance confirmed if the *p*–value is under 0.05. As shown in Table 3, all independent variables exert a significant influence on the response. Similarly, the interaction terms–concentration–pH, concentration–time, pH–time, concentration–concentration, pH–pH, and time–time also exhibit *p*–value < 0.05, demonstrating that both linear and interaction effects are statistically significant.

Table 2: Experimental design for the three independent variables.

Run	PRD Concentration (mg/L)	pH	Time (min)	Response (%)		Residual
				Actual	Predicted	
1	50	2	90	72.11	72.24	-0.13
2	50	2	30	87.11	86.39	0.72
3	30	5.5	60	97.80	96.86	0.94
4	10	5.5	60	86.21	86.24	-0.03
5	30	5.5	90	81.67	83.49	-1.82
6	50	9	90	62.68	61.63	1.05
7	30	5.5	30	77.68	75.96	1.72
8	30	2	60	89.22	90.38	-1.16
9	10	9	30	43.25	43.10	0.15
10	10	2	90	69.61	68.02	1.59
11	10	2	30	48.78	49.80	-1.02
12	30	5.5	60	95.34	96.86	-1.52
13	50	5.5	60	99.14	99.21	-0.07
14	30	5.5	60	98.81	96.86	1.95
15	30	9	60	82.78	81.72	1.06
16	30	5.5	60	92.14	96.86	-4.72
17	30	5.5	60	98.62	96.86	1.76
18	30	5.5	60	98.64	96.86	1.78
19	50	9	30	63.23	64.80	-1.57
20	10	9	90	71.61	72.30	-0.69

Table 3: ANOVA analysis for quadratic models.

Source	Sum of squares	df	Mean Square	F-value	*p*-value	
Model	5385.01	9	598.33	114.12	< 0.0001	significant
A. Concentration	420.03	1	420.03	80.12	< 0.0001	significant
B. pH	187.32	1	187.32	35.73	0.0001	significant
C. Time	141.60	1	141.60	27.01	0.0004	significant
AB	110.86	1	110.86	21.14	0.0010	significant
AC	523.91	1	523.91	99.93	< 0.0001	significant
BC	60.39	1	60.39	11.52	0.0068	significant
A^2	46.97	1	46.97	8.96	0.0135	significant
B^2	321.22	1	321.22	61.27	< 0.0001	significant
C^2	807.21	1	807.21	153.96	< 0.0001	significant
Residual	52.43	10	5.24			
Lack of Fit	16.89	5	3.38	0.4754	0.7831	not significant
Pure Error	35.53	5	7.11			
Core Total	5437.43	19				
Std. Dev	2.29					
Mean	80.82					
C.V. %	2.83					
R^2	0.9904					
Adjusted R^2	0.9817					
Predicted R^2	0.9503					
Adeq Precision	34.6561					

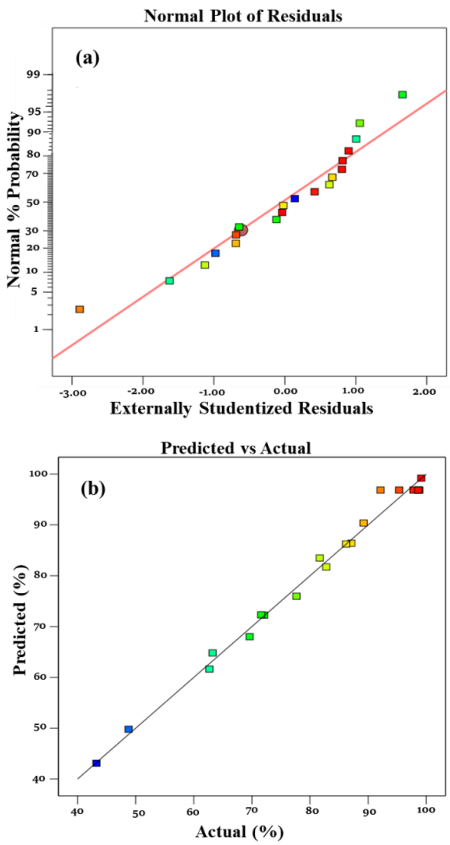

Figure 6: Illustration of the (a) normal plot of residual and (b) predicted vs. actual.

The coefficient of determination (R^2) of 0.9904, which is close to 1, indicates an excellent correlation between the experimental and predicted data. Moreover, the small difference between the adjusted R^2 and predicted R^2 values (< 0.2) confirms the high predictive accuracy of the model [43]. The Adeq Precision value, which exceeds the acceptable threshold (> 4), further supports the reliability of the model for optimization and prediction purposes.

The statistical validity of the model is further supported by the Normal Plot of Residuals (Figure 6(a)), where most residual points lie close to the straight line, confirming a normal distribution of errors. Additionally, the plot of Predicted versus Actual values (Figure 6(b)) shows data points clustered near the diagonal line, demonstrating excellent correlation and predictive reliability. Points above the line indicate underprediction, whereas those below indicate overprediction by the model [44].

Equations in actual factor form are presented to facilitate practical predictions under experimental conditions. The quadratic regression equation derived from Analysis of Variance (ANOVA) to predict the degradation efficiency (E) is expressed as follows Equation (1):

$$E(\%) = -42.523 + 2.046A + 8.494B + 2.671C - 0.053AB - 0.013AC + 0.026BC - 0.010A^2 - 0.882B^2 - 0.019C^2 \quad (1)$$

The 3D response surface and contour plots illustrating the interactions between concentration–pH, concentration–time, and pH–time are presented in Figure 7(a)–(c).

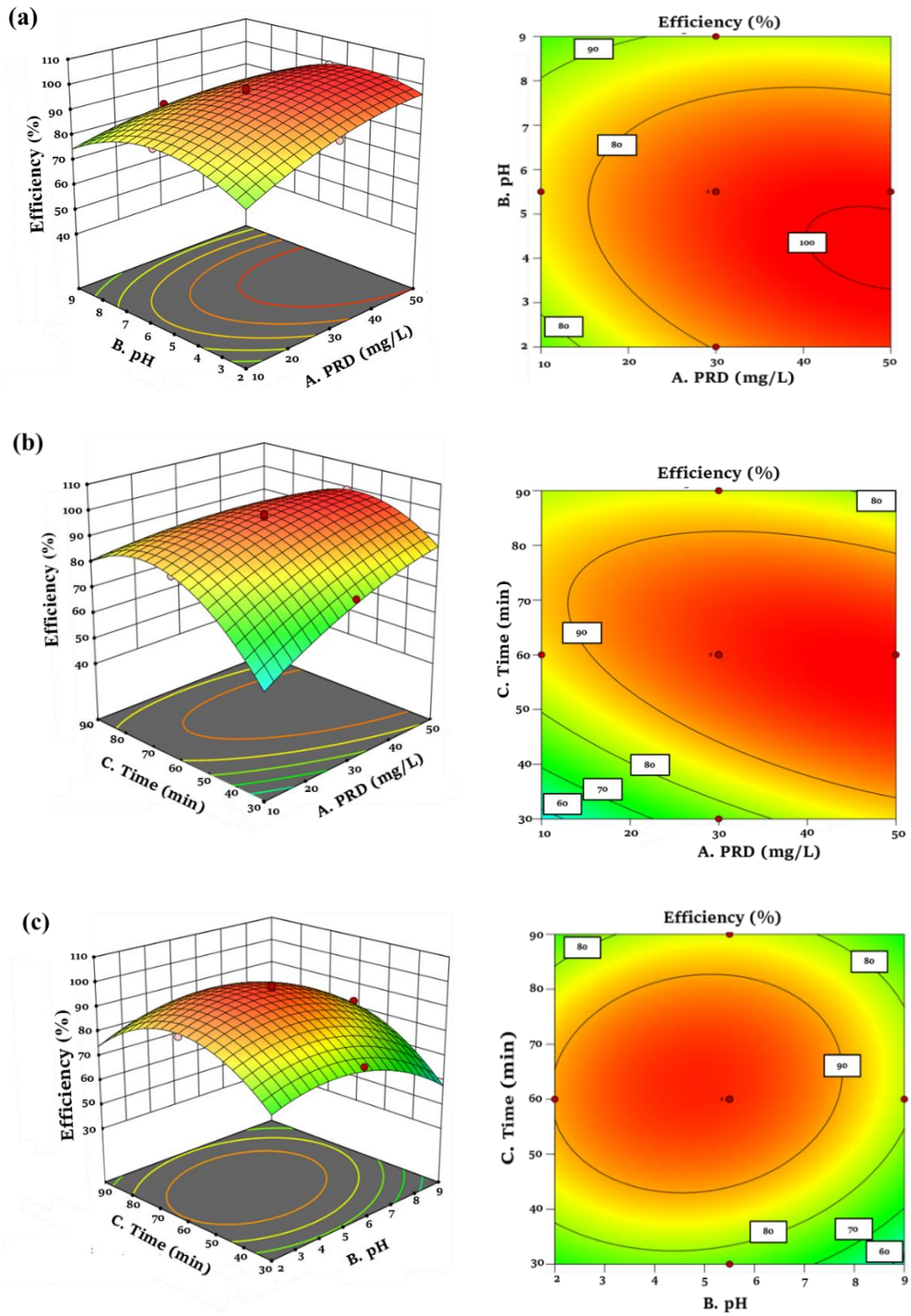

Figure 7: Interaction of independent variables (a) concentration-pH, (b) concentration–time and (c) pH–time.

In general, increasing PRD concentration, pH, and irradiation time enhances degradation efficiency up to an optimum point, after which efficiency declines. The red regions represent the highest degradation efficiencies, whereas the green areas correspond to the lowest. At excessively high PRD concentrations, the radiation source may be hindered from reaching the catalyst surface, reducing the generation of reactive radicals and thereby lowering photocatalytic performance [45].

In the initial stage, the degradation rate rises sharply due to abundant active sites available on the catalyst surface. However, beyond the optimal conditions, degradation efficiency decreases markedly, likely due to the accumulation of intermediate compounds and byproducts formed during the reaction. Extended irradiation times can also reduce efficiency because of increased opportunities for free radical recombination [46].

Surface charge plays a crucial role in determining the electrostatic interactions that occur on the composite surface during the degradation process. Since pH strongly influences surface charge behavior, it directly affects photocatalytic degradation efficiency. PRD is an anionic compound containing sulfonate groups ($–SO_3^-$), which render it water–soluble and negatively charged. The point of zero charge (pHpzc) of the $MnFe_2O_4$/Chitosan–Alginate@TiO_2 composite was determined to be 6.35 (Figure 8).

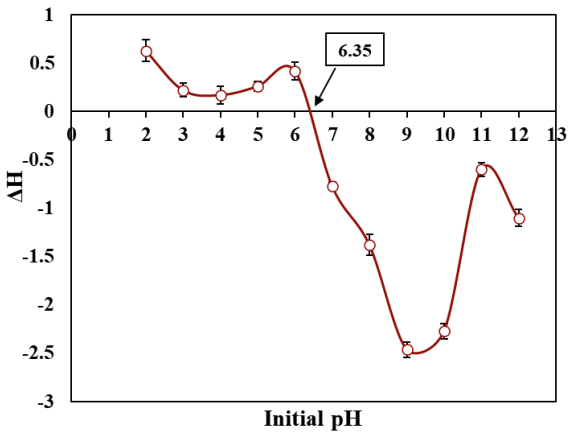

Figure 8: pHpzc $MnFe_2O_4$/Chitosan–Alginate@TiO_2.

The RSM–predicted optimum pH of 3.3 is well below the determined pHpzc of 6.35. This confirms that under acidic conditions, the catalyst surface is positively charged, favoring the adsorption and subsequent degradation of the anionic PRD dye molecules, which is consistent with the model's findings. Similar findings were reported by other researchers, where PRD degradation using EDTA–modified $BiFeO_3$ was most effective at pH 3 [4].

Table 4 summarizes the verification of the optimal degradation. The experimental degradation efficiency yielded a desirability value of 1. A desirability value approaching unity indicates that the model successfully predicts the optimal process conditions with high accuracy. The verification was conducted to evaluate the suitability of the optimum conditions predicted by RSM relative to the actual results [43]. The optimum parameters obtained from the RSM model were a PRD concentration of 45 mg/L, pH 3.3, and an irradiation time of 59 min. The verification process was carried out by running three experiments under the optimum conditions. The actual results were then compared with the predicted values. The mean of the actual degradation efficiency of 99.33% was very close to the predicted value of 99.71%, with a deviation of less than 1%. This indicates that the developed RSM model has high accuracy.

Table 4: Verification of the optimized conditions.

Actual (%)	Mean (%)	Std Dev	Predicted (%)	Deviation
98.67 99.40 99.92	99.33	2.28	99.71	0.38

Total Organic Carbon (TOC) analysis was performed to determine whether the photocatalytic process led only to structural transformation or complete mineralization of PRD. TOC measurements distinguish between mere decolorization and actual mineralization, where organic carbon is converted into inorganic species. In this study, a TOC removal efficiency of 84.30% was achieved, indicating that PRD underwent substantial mineralization into CO_2 and H_2O. This relatively high removal rate confirms that the $MnFe_2O_4$/Chitosan–Alginate@TiO_2 composite effectively generates Reactive Oxygen Species (ROS) capable of decomposing PRD. Furthermore, the composite exhibited superior mineralization performance compared to previously reported catalysts, such as CeO_2/BiOBr, which achieved 53.55% Congo red degradation [47], and Clay/$MnFe_2O_4$, which reached 83% for Methyl violet dye [26].

The photocatalytic degradation mechanism of PRD using the $MnFe_2O_4$/Chitosan–Alginate@TiO_2 composite can be summarized as follows [48].

$MnFe_2O_4/CA@TiO_2 + hv \rightarrow e^- + h^+$ (2)

$H_2O + h^+ \rightarrow \bullet OH + H^+$ (3)

$O_2 + e^- \rightarrow \bullet O_2^-$ (4)

$\bullet O_2^- + H_2O \rightarrow H_2O_2 \rightarrow 2\bullet OH$ (5)

Under light irradiation (hν), $MnFe_2O_4$/Chitosan–Alginate@TiO_2 composite experiences photoexcitation, where electrons (e^-) are promoted from the TiO_2 valence band to the conduction band, resulting in the formation of holes (h^+) in the valence band (Equation (2)). $MnFe_2O_4$ acts as an effective charge mediator by enhancing electron–hole separation and inhibiting their recombination. The photogenic holes (h^+) then react with H_2O molecules, producing highly reactive hydroxyl radicals (•OH) (Equation 3). Meanwhile, electrons in the conduction band react with dissolved oxygen (O_2) to form superoxide radicals ($\bullet O_2^-$) (Equation 4). The species ($\bullet O_2^-$) then undergoes a chain reaction with H_2O to produce hydrogen peroxide (H_2O_2), which then decomposes into additional hydroxyl radicals, as expressed in Equation (5).

The role of the chitosan–alginate biopolymer matrix is not only as a structural support but also as an initial adsorption medium for PRD via electrostatic interactions. The simultaneous formation of hydroxyl radicals (•OH) and superoxide radicals ($\bullet O_2^-$) plays a dominant role in the PRD oxidation process. These radical attacks cause the chromophore bond to break, the aromatic ring to open, and the formation of simpler intermediate compounds, ultimately producing CO_2, H_2O and other non–toxic compounds as the final mineralization products in Equation 6 [48], [49].

$PRD + \bullet OH + \bullet O_2^- \rightarrow CO_2 + H_2O +$ non–toxic compounds (6)

The comparison of the average PRD degradation values, pure TiO_2, $MnFe_2O_4$/Chitosan–Alginate, and $MnFe_2O_4$/Chitosan–Alginate@TiO_2 at the same conditions (optimum conditions of degradation) showed efficiencies of 55.67%, 72.45%, and 99.33%, respectively. These findings indicate that the integration of TiO_2 into the $MnFe_2O_4$/Chitosan–Alginate significantly improves its degradation ability.

The PRD degradation efficiency by $MnFe_2O_4$/Chitosan–Alginate@TiO_2 composite showed better performance than ZnO–natural zeolite nano-sized composite, which reached 96.23% after 120 min of irradiation [50]. Its performance was also comparable to EDTA-modified $BiFeO_3$, which was able to degrade PRD up to 99% [4], but the method required a longer time (120 min) and used a lower initial PRD concentration (20 mg/L). These findings suggest that $MnFe_2O_4$/Chitosan–Alginate@TiO_2 composite was proven to be able to provide high degradation efficiency for PRD in a shorter time, even though it was used at higher pollutant concentrations.

3.3 *Reusability of $MnFe_2O_4$/Chitosan–Alginate@TiO_2 Composite*

The reusability of the catalyst is an important parameter for assessing its practical applicability and long-term stability. The degradation experiments were conducted using a PRD concentration of 45 mg/L at pH 3.3 with an irradiation time of 59 min. The catalyst was subjected to six consecutive reuse cycles, achieving degradation efficiencies of 98.54%, 97.56%, 95.89%, 93.40%, 92.11%, and 91.56% (Figure 9). After six cycles, the overall degradation efficiency decreased by only 6.98%, remaining above 85% throughout. This finding indicates that the catalyst did not experience a significant decrease in activity.

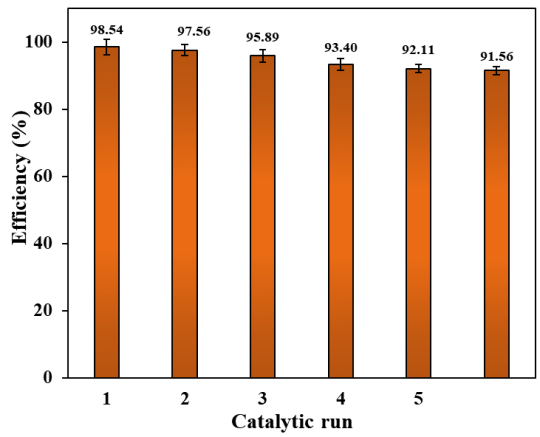

Figure 9: Reusability of photocatalytic degradation PRD using $MnFe_2O_4$/Chitosan–Alginate@TiO_2 composite.

This excellent reusability demonstrates that the $MnFe_2O_4$/Chitosan–Alginate@TiO_2 composite possesses high structural integrity and chemical stability, and resists activity loss due to leaching during the photocatalytic process. The ability to maintain high activity over multiple cycles also highlights its economic advantages for large–scale or industrial applications [51]. The minor reduction in photocatalytic efficiency after multiple cycles is likely due to the buildup of remaining contaminants on the catalyst surface, which blocks active sites and limits both light absorption and interaction with pollutants.

In addition, partial catalyst loss during recovery between cycles may also contribute to the observed decrease in performance [52], [53].

Overall, the $MnFe_2O_4$/Chitosan–Alginate@TiO_2 composite has high applicability potential in real wastewater treatment because it is easily separated magnetically, can be reused, works effectively under mild operating conditions, and is able to handle higher pollutant concentrations, so it is worthy of consideration for implementation in industrial-scale wastewater treatment plants.

Figure 10 shows that the catalyst material can be effectively attracted using a magnet, demonstrating the strong magnetic properties of the $MnFe_2O_4$/Chitosan–Alginate@TiO_2 composite. This capability is very advantageous because it allows for quick and easy separation of the catalyst from the solution, without the need for filtration or centrifugation. This also confirms that the catalyst is reusable for subsequent degradation cycles.

Figure 10: PRD before and after degradation.

3.4 *Ecotoxicity test*

Ecotoxicity testing was carried out to evaluate whether the degradation products generated after photocatalysis pose any harmful effects on living organisms. Three experimental treatments were prepared: 1) distilled water as a control, 2) PRD solution treated with the $MnFe_2O_4$/Chitosan–Alginate@TiO_2 composite (treated water), and 3) PRD solution (5 mg/L) without treatment (untreated water). Each treatment was replicated three times, and the germination of green gram seeds was observed. The comparative analysis of seed growth across the three treatments provided insight into the potential toxicity of the degradation byproducts and the suitability of the treated water for safe agricultural or environmental reuse.

As shown in Figure 11, clear differences were observed in green gram seed germination after four days among the three treatments. Seeds exposed to untreated PRD solution exhibited poor growth, whereas those germinated in treated water showed growth comparable to the control group. In untreated water, more than 50% of seeds do not experience growth. The dark coloration of the plant roots was attributed to the uptake of dye molecules. This indicates that photocatalytic treatment effectively reduces the toxicity of PRD.

The inhibition of germination in untreated PRD media can be attributed to the toxic nature of dye molecules, which may damage cell membranes, disrupt enzymatic activity, and interfere with DNA function in plant tissues. Additionally, the intense coloration of dye solutions can limit oxygen solubility, thereby restricting root respiration. These findings confirm that photocatalytically treated water containing PRD can be safely reused for agricultural purposes.

Comparable studies have reported similar effects of dye type on seed germination, where the germination rates of mung beans exposed to Methyl Orange, Eriochrome Black T (EBT), and Eosin Y (EY) dyes were 29.3%, 37.3%, and 34.67%, respectively, compared to 96.4% in the control [6]. After four days, plants grown in untreated PRD solution exhibited the shortest shoot lengths, further confirming the toxicity of the undegraded dye.

4 Conclusions

The $MnFe_2O_4$/Chitosan–Alginate@TiO_2 composite was successfully synthesized and effectively applied for Procion red MX-5B dye (PRD) degradation. The material exhibits a narrow band gap, enabling efficient visible-light absorption, and possesses magnetic properties that facilitate its recovery and reuse. In the $MnFe_2O_4$/Chitosan–Alginate@TiO_2 heterojunction system. Electrons from $MnFe_2O_4$ move to TiO_2, while holes from TiO_2 move to $MnFe_2O_4$, thereby suppressing charge recombination. This efficient charge separation produces active radicals such as $\bullet O_2^-$ and •OH, which play a role in increasing the efficiency of pollutant degradation.

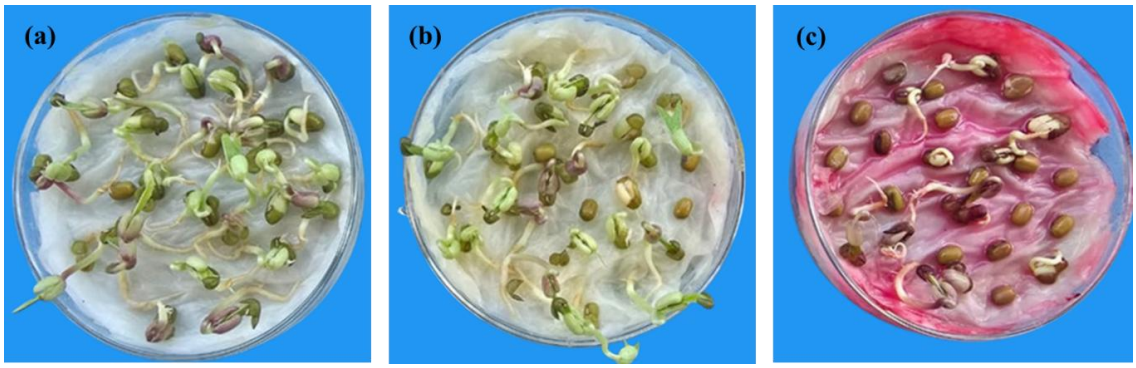

Figure 11: Ecotoxicity test using green gram seeds: (a) control, (b) treated water, and (c) untreated water on day 4.

Using a Central Composite Design (CCD) within Response Surface Methodology (RSM) to optimize PRD degradation, it was found that a quadratic model best described the data, achieving an R^2 of 0.9904. The p-values (<0.05) for all individual and interaction terms indicate significant effects, while the small deviation between experimental and predicted results validates the model's reliability. The optimal degradation conditions were achieved at a PRD concentration of 45 mg/L, pH 3.3, and irradiation time of 59 min, yielding a degradation efficiency of 99.71%. The composite showed excellent stability, with only a 6.98% decrease in activity after six reuse cycles. Additionally, the TOC removal of 84.30% confirmed extensive mineralization, and ecotoxicity tests revealed that the treated water supported healthy growth of green gram seeds.

Acknowledgments

Gratitude is expressed to the Directorate of Research and Community Service, Federal Directorate of Research and Development, Ministry of Higher Education, Science, and Technology, Indonesia, for funding the Fundamental scheme with contract No. 109/C3/DT.05.00/PL/2025 for the 2025 year.

Author Contributions

P.L.H.: conceptualization, investigation, reviewing and editing; A.R.: methodology, writing an original draft; S.: validation, data analysis; D.: data curation, reviewing and editing; N.A.: formal analysis, reviewing and editing; A.F.: methodology, validation, A.: methodology, project administration.

Conflicts of Interest

The authors declare no conflict of interest.

References

[1] A. Iqajtaoune, M. Taibi, H. Saufi, B. Aouan, and L. Boudad, "Enhanced removal of Methylene blue and Procion deep red H-EXL dyes from aqueous environments by modified-bentonite: Isotherm, kinetic, and thermodynamic," *Desalination Water Treatment*, vol. 320, Oct. 2024, Art. no. 100607, doi: 10.1016/j.dwt.2024.100607.

[2] V. Katheresan, J. Kansedo, and S. Y. Lau, "Efficiency of various recent wastewater dye removal methods: A review," *Journal of Environmental Chemical Engineering*, vol. 6, no. 4, pp. 4676–4697, Aug. 2018, doi: 10.1016/j.jece.2018.06.060.

[3] P. S. Thue et al., "Intercalation of organosilane in clay mineral for the removal of Procion red MX-5B: Investigational and theoretical studies," *Separation and Purification Technology*, vol. 347, Nov. 2024, Art. no. 127491, doi: 10.1016/j.seppur.2024.127491.

[4] E. Da Cruz Severo et al., "Improved catalytic activity of EDTA-modified $BiFeO_3$ powders for remarkable degradation of Procion red by heterogeneous photo-Fenton process," *Journal of Environmental Chemical Engineering*, vol. 8, no. 4, Aug. 2020, Art. no. 103853, doi: 10.1016/j.jece.2020.103853.

[5] R. Al-Tohamy et al., "A critical review on the treatment of dye-containing wastewater: Ecotoxicological and health concerns of textile dyes and possible remediation approaches for environmental safety," *Ecotoxicology and*

Environmental Safety, vol. 231, Feb. 2022, Art. no. 113160, doi: 10.1016/j.ecoenv.2021.113160.

[6] S. Abhirami, G. Thiruppathi, M. S. Ola, M. Arunkumar, P. Sundararaj, and P. V. Joseph, "Eco-conscious synthesis of chitosan-reduced magnetic Iron oxide nanocomposite from crab shell waste for photocatalytic degradation of textile dyes: Ecotoxicity insights," *Journal of Water Process Engineering*, vol. 78, Oct. 2025, Art. no. 108651, doi: 10.1016/j.jwpe.2025.108651.

[7] M. C. Ribas et al., "Adsorption of Procion red MX-5B dye from aqueous solution using homemade peach and commercial activated carbons," *Applied Water Science*, vol. 10, no. 6, pp. 1–13, Jun. 2020, doi: 10.1007/s13201-020-01237-9.

[8] H. Chen, W. Chen, Y. Lin, Y. Xie, S. H. Liu, and J. Yin, "Visible and near-infrared light activated azo dyes," *Chinese Chemical Letters*, vol. 32, no. 8, pp. 2359–2368, Aug. 2021, doi: 10.1016/j.cclet.2021.03.020.

[9] P. Tao and Y. Wang, "Enhanced photocatalytic performance of W-doped TiO_2 nanoparticles for treatment of Procion red MX-5B azo dye in textile wastewater," *International Journal of Electrochemical Science*, vol. 18, no. 9, Sep. 2023, Art. no. 100261, doi: 10.1016/j.ijoes.2023.100261.

[10] S. Cotillas, D. Clematis, P. Cañizares, M. P. Carpanese, M. A. Rodrigo, and M. Panizza, "Degradation of dye Procion red MX-5B by electrolytic and electro-irradiated technologies using diamond electrodes," *Chemosphere*, vol. 199, pp. 445–452, May 2018, doi: 10.1016/j.chemosphere.2018.02.001.

[11] P. Hua et al., "Adsorption of Acid green and Procion red on a magnetic geopolymer based adsorbent: Experiments, characterization and theoretical treatment," *Chemical Engineering Journal*, vol. 383, Mar. 2020, Art. no. 123113, doi: 10.1016/j.cej.2019.123113.

[12] D. Tonato et al., "Residual biomass of *Nigrospora* sp. from process of the microbial oil extraction for the biosorption of Procion red H–E7B dye," *Journal of Water Process Engineering*, vol. 31, Oct. 2019, Art. no. 100818, doi: 10.1016/j.jwpe.2019.100818.

[13] A. Benalia, K. Derbal, O. Baatache, C. Lehchili, A. Khalfaoui, and A. Pizzi, "Removal of dyes from water using aluminum-based water treatment sludge as a low-cost coagulant: Use of Response Surface Methodology," *Water*, vol. 16, no. 10, May 2024, Art. no. 1400, doi: 10.3390/w16101400.

[14] G. Mugaishudeen, M. Harish, and R. Singaraja gopal, "Removal of Methylene blue and Congo red from the wastewater in a jet loop reactor using ozone and activated carbon," *Desalination Water Treatment*, vol. 319, Jul. 2024, Art. no. 100471, doi: 10.1016/j.dwt.2024.100471.

[15] H. Tang et al., "Recent advances in nanoscale zero-valent iron-based materials: Characteristics, environmental remediation and challenges," *Journal of Cleaner Production*, vol. 319, Oct. 2021, Art. no. 128641, doi: 10.1016/j.jclepro.2021.128641.

[16] A. G. El-Shamy, "Novel in-situ synthesis of nano-silica (SiO_2) embedded into polyvinyl alcohol for dye removal: Adsorption and photo-degradation under visible light," *Polymer*, vol. 242, Mar. 2022, Art. no. 124579, doi: 10.1016/j.polymer.2022.124579.

[17] A. Smýkalová, B. Sokolová, K. Foniok, V. Matejka, and P. Praus, "Photocatalytic degradation of selected pharmaceuticals using g-C_3N_4 and TiO_2 nanomaterials," *Nanomaterials*, vol. 9, no. 9, Sep. 2019, Art. no. 1194, doi: 10.3390/nano9091194.

[18] L. Mao, Y. Lian, Y. Ma, C. Cui, Z. Chen, and Y. Zhang, "Innovative TiO_2-doped polyvinyl alcohol sponge for efficient oil–water separation and dye degradation in wastewater treatment," *Chemical Engineering Science*, vol. 298, Oct. 2024, Art. no. 120389, doi: 10.1016/j.ces.2024.120389.

[19] F. C. Souza, C. R. Bellato, J. de O. M. Neto, S. O. Ferreira, and E. N. D. de Araújo, "Preparation and evaluation of magnetic iron oxide-MgCeAl lamellar composite-TiO_2 in the photocatalytic degradation of Methylene blue dye," *Colloids and Surfaces A: Physicochemical and Engineering Aspects*, vol. 691, Jun. 2024, Art. no. 133894, doi: 10.1016/j.colsurfa.2024.133894.

[20] E. Turcu, C. G. Coromelci, V. Harabagiu, and M. Ignat, "Enhancing the photocatalytic activity of TiO_2 for the degradation of Congo red dye by adjusting the ultrasonication regime applied in its synthesis procedure," *Catalysts*, vol. 13, no. 2, Feb. 2023, Art. no. 13020345, doi: 10.3390/catal13020345.

[21] L. El Mersly, E. M. El Mouchtari, M. Belghiti, K. Belkodia, M. A. Edaala, S. Briche, A. A. Tahiri, and S. Rafqah, "Development of a new

composite LDH/TiO_2-3D for degradation of sulfaguanidine under UV and visible light: Experimental design, kinetic and mechanisms," *Journal of Environmental Chemical Engineering*, vol. 11, no. 6, Dec. 2023, Art. no. 111038, doi: 10.1016/j.jece.2023.111038.

[22] E. Mohammed-Amine et al., "Novel sol-gel synthesis of TiO_2/$BiPO_4$ composite for enhanced photocatalytic degradation of carbamazepine under UV and visible light: Kinetic, identification of photoproducts and mechanistic insights," *Journal of Water Process Engineering*, vol. 70, Feb. 2025, Art. no. 107098, doi: 10.1016/j.jwpe.2025.107098.

[23] P. L. Hariani, S. Salni, M. V. Kimur, N. Hidayati, and E. Elfita, "Fabrication of $NiFe_2O_4$/SiO_2/TiO_2 magnetic composite for effective photodegradation of Congo red dye," *Indonesian Journal of Chemistry*, vol. 25, no. 3, pp. 665–679, Jun. 2025, doi: 10.22146/ijc. 94143.

[24] G. C. de Cristo Borges et al., "Magnetic heterostructures of $NiFe_2O_4$ and TiO_2: Pechini synthesis, characterization and photocatalytic performance in arsenite oxidation," *Journal of Water Process Engineering*, vol. 56, Dec. 2023, Art. no. 104352, doi: 10.1016/j.jwpe.2023. 104352.

[25] S. Kafash, H. M. Moghaddam, S. F. H. Karouei, and A. B. Khatibani, "Facile template-free synthesis of PANI/TiO_2 nanocomposite with enhanced photocatalytic activity for Methyl orange degradation," *Materials Science and Engineering: B*, vol. 321, Nov. 2025, Art. 118548, doi: 10.1016/j.mseb.2025.118548.

[26] H. Madhu and S. Rajendra Prasad, "Synthesis and Characterization of $MnFe_2O_4$ and Clay/$MnFe_2O_4$ using neem leaves for photodegradation and radical scavenging studies," *Sustainable Chemistry One World*, vol. 7, Sep. 2025, Art. no. 100081, doi: 10.1016/j.scowo.2025.100081.

[27] D. Kanakaraju, M. H. bin Ya, Y. C. Lim, and A. Pace, "Combined Adsorption/photocatalytic dye removal by copper-titania-fly ash composite," *Surfaces and Interfaces*, vol. 19, Jun. 2020, Art. no. 100534, doi: 10.1016/ j.surfin.2020.100534.

[28] H. Shehzad et al., "Modified alginate-chitosan-TiO_2 composites for adsorptive removal of Ni(II) ions from aqueous medium," *International Journal of Biological Macromolecules*, vol. 194, pp. 117–127, Jan. 2022, doi: 10.1016/j.ijbiomac.2021.11.140.

[29] D. L. Puspitarum et al., "Novel magnetically recoverable $MnFe_2O_4$/TiO_2 nanocomposites synthesized using green route for photocatalytic degradation of Methylene blue," *Water Cycle*, vol. 6, pp. 49–60, Jan. 2025, doi: 10.1016/j.watcyc.2024.11.001.

[30] A. Grzegórska, J. C. Ofoegbu, L. Cervera-Gabalda, C. Gómez-Polo, D. Sannino, and A. Zielińska-Jurek, "Magnetically recyclable TiO_2/MXene/$MnFe_2O_4$ photocatalyst for enhanced peroxymonosulphate-assisted photocatalytic degradation of carbamazepine and ibuprofen under simulated solar light," *Journal of Environmental Chemical Engineering*, vol. 11, no. 5, Oct. 2023, Art. no. 110660, doi: 10.1016/j.jece.2023.110660.

[31] X. Cao, H. Liu, B. Wang, C. Zhang, and S. Yao, "Effective removal of Cd(II) from aqueous solution by $MnFe_2O_4$ composite modified by surfactant," *Desalination Water Treatment*, vol. 262, pp. 168–179, Jun. 2022, doi: 10.5004/dwt. 2022.28438.

[32] H. Hamedi, S. Moradi, A. E. Tonelli, and S. M. Hudson, "Preparation and characterization of chitosan–Alginate polyelectrolyte complexes loaded with antibacterial thyme oil nanoemulsions," *Applied Sciences*, vol. 9, no. 18, Sep. 2019, Art. no. 3933, doi: 10.3390/ APP9183933.

[33] A. Karim, A. Rehman, J. Feng, A. Noreen, E. Assadpour, M. S. Kharazmi, Z. Lianfu, S. M. Jafari, "Alginate-based nanocarriers for the delivery and controlled-release of bioactive compounds," *Advances in Colloid and Interface Science,* vol. 307, Sep. 2022, Art. no. 102744, doi: 10.1016/j.cis.2022.102744.

[34] L. H. Monroy, J. R. Tavares, and M. J. Dumont, "Photodegradation of ciprofloxacin using an alginate/TiO_2 hydrogel for water remediation," *Journal of Environmental Chemical Engineering*, vol. 13, no. 2, Apr. 2025, Art. no. 115868, doi: 10.1016/j.jece.2025.115868.

[35] N. Ahmia, M. Benamira, L. Messaadia, H. Lahmar, M. Trari, and I. Avramova, "Photocatalytic degradation of an organic pollutant using $ZnMn_2O_4$/TiO_2 heterojunction under solar light," *Materials Science and Engineering: B*, vol. 322, Dec. 2025, Art. no. 118626, doi: 10.1016/j.mseb.2025.118626.

[36] Y. Zhang et al., "Construction of titanium dioxide/cadmium sulfide heterojunction on

carbon fibers as weavable photocatalyst for eliminating various contaminants," *Journal of Colloid Interface Science*, vol. 561, pp. 307–317, Mar. 2020, doi: 10.1016/j.jcis.2019.10.105.

[37] Q. Hu et al., "Constructing carbon microspheres/$MnFe_2O_4$/g-C_3N_4 composite photocatalysts for enhanced photocatalytic activity under visible light irradiation," *Inorganic Chemistry Communications*, vol. 134, Dec. 2021, Art. no. 108947, doi: 10.1016/j.inoche.2021.108947.

[38] A. M. Ahmed et al., "Removal of phosphate from wastewater using zirconium/iron embedded chitosan/alginate hydrogel beads: An experimental and computational perspective," *International Journal of Biological Macromolecules*, vol. 281, Nov. 2024, Art. no. 136431, doi: 10.1016/j.ijbiomac.2024.136431.

[39] G. Zerjav, K. Zizek, J. Zavasnik, and A. Pintar, "Brookite vs. rutile vs. anatase: What's behind their various photocatalytic activities?," *Journal of Environmental Chemical Engineering*, vol. 10, no. 3, Jun. 2022, Art. no. 107722, doi: 10.1016/j.jece.2022.107722.

[40] E. Aghababaei, M. Alizadeh, and A. Bahrami, "Synthesis and characterization of Ce-doped TiO_2/Cu-doped Fe_3O_4 heterogeneous photocatalyst for antibacterial applications and visible-light photocatalytic degradation of Methylene blue," *Ceramics International*, vol. 51, no. 21, pp. 33740–33758, Sep. 2025, doi: 10.1016/j.ceramint.2025.05.109.

[41] C. Mohanty, P. P. Mishra, A. Samal, N. Das, and A. K. Behera, "Design of inexpensive, magnetically separable $MnFe_2O_4$/poly meta-amino phenol (PmAP) heterostructure: Catalyst for bisphenol A & reactive blue 19 mineralisation," *Environmental Science: Advances*, vol. 3, no. 4, pp. 561–571, Mar. 2024, doi: 10.1039/d3va00394a.

[42] T. Xiang et al., "Efficient degradation of organic pollutants by ozone oxidation catalyzed by chitosan-derived N-doped carbon and $MnFe_2O_4$ co-doped CuS," *International Journal of Biological Macromolecules*, vol. 319, Aug. 2025, Art. no. 145671, doi: 10.1016/j.ijbiomac.2025.145671.

[43] T. Pahasup-anan, K. Suwannahong, P. Kampeerapappun, R. Rangkupan, and W. Dechapanya, "Conditional optimization on the photocatalytic degradation removal efficiency of formaldehyde using TiO_2 – nylon 6 electrospun composite membrane," *Applied Science and Engineering Progress*, vol. 18, no.1, Jan. 2025, Art. no. 7509, doi: 10.14416/j.asep.2024.07.012.

[44] U. Farooq et al., "Successive evaluation of the green synthesized rare earth metal oxide CeO_2 nanoparticles for the photo-induced degradation of Methylene blue and CO_2 photoreduction: Optimization of the reaction parameters by RSM-CCD model," *Journal of the Taiwan Institute Chemical Engineers*, vol. 174, Sep. 2025, Art. no. 106220, doi: 10.1016/j.jtice.2025.106220.

[45] B. M. Quy et al., "Photocatalytic degradation performance of a chitosan/ZnO-Fe_3O_4 nanocomposite over cationic and anionic dyes under visible-light irradiation," *RSC Advances*, vol. 15, no. 3, pp. 1590–1603, Jan. 2025, doi: 10.1039/d4ra08262a.

[46] A. Ajami, S. Sheibani, and A. Ataie, "S-scheme $CoFe_2O_4$/g-C_3N_4 nanocomposite with high photocatalytic activity and antibacterial capability under visible light irradiation," *Journal of Materials Research and Technology*, vol. 30, pp. 2168–2185, May 2024, doi: 10.1016/j.jmrt.2024.04.010.

[47] X. Chen et al., "Peroxymonosulfate activation using $MnFe_2O_4$ modified biochar for organic pollutants degradation: Performance and mechanisms," *Separation and Purification Technology*, vol. 308, Mar. 2023, Art. no. 122886, doi: 10.1016/j.seppur.2022.122886.

[48] A. Boucherdoud et al., "Polyaniline/cupric oxide organometallic nanocomposites as a sonocatalyst for the degradation of methylene blue: Experimental study, RSM optimization, and DFT analysis," *Journal of Organometallic Chemistry*, vol. 1022, Dec. 2024, Art. no. 123386, doi: 10.1016/j.jorganchem.2024.123386.

[49] G. Sofia, C. Koventhan, S. Kanmani, A. Lo, "Green synthesized rGO/TiO_2/g-C_3N_4 nanocomposites via *Plectranthus amboinicus* extract for efficient photocatalytic degradation of Methylene blue: RSM optimization, antimicrobial and phytotoxicity assessment." *Journal of Environmental Chemical Engineering,* vol. 13, Feb. 2025, Art. no. 115267, doi: 10.1016/j.jece.2024.115267.

[50] T. E. Agustina, E. Melvita, D. Bahrin, R. Gayatri, and I. F. Purwaningtyas, "Synthesis of nano-photocatalyst ZnO-natural zeolite to degrade Procion red," *International Journal of Technology,* vol. 11, no. 3, pp. 472–481, Apr. 2020, doi: 10.14716/ijtech.v11i3.3800.

[51] S. L. Chiam, C. P. Leo, S. Y. Pung, and W. L. Ang, "Modulation of MnO_2-BiOCl photocatalyst *Solid State Sciences*, vol. 160, Feb. 2025, Art. no. 107831, doi: 10.1016/j.solidstatesciences.2025.107831.

[52] M. Esmati, A. Allahresani, and A. Naghizadeh, "Synthesis and characterization of Graphitic Carbon Nitride/Mesoporous Nano-Silica (g-C_3N_4/KCC-1) nanocomposite as a novel highly efficient and recyclable photocatalyst for degradation of antibiotic in aqueous solution," *Research on Chemical Intermediates*, vol. 47, no. 4, pp. 1447–1469, Apr. 2021, doi: 10.1007/s11164-020-04358-7.

[53] T. Q. Thao, N. T. T. Hien, P. T. Lam, and N. N. Huy, "Exploring, the mechanism for the photocatalytic degradation of Oxytetracycline in water using TiO_2 and supplementary Oxidants," *Applied Science and Engineering Progress*, vol. 18, no. 3, Jul. 2025, Art. no. 7651, doi: 10.14416/j.asep.2024.11.007.